

Capturing structural changes of photosystem II using time-resolved serial femtosecond crystallography with proper flash excitations

Honjie Li

Okayama University <https://orcid.org/0000-0002-8827-0093>

Yoshiki Nakajima

Research Institute for Interdisciplinary Science and Graduate School of Natural Science and Technology,
Okayama University <https://orcid.org/0000-0002-0529-8075>

Takashi Nomura

University of Hyogo

Michihiro Sugahara

RIKEN

Shinichiro Yonekura

Okayama University

Siu Kit Chan

Okayama University

Takanori Nakane

MRC laboratory of molecular biology <https://orcid.org/0000-0003-2697-2767>

Takahiro Yamane

Okayama University

Yasufumi Umena

Okayama University

Mamoru Suzuki

Osaka University

Tetsuya Masuda

Kyoto University

Taiki Motomura

Okayama university

Hisashi Naitow

RIKEN SPring-8 Center <https://orcid.org/0000-0001-7567-231X>

Yoshinori Matsuura

RIKEN SPring-8 Center

Tetsunari Kimura

Kobe University

Kensuke Tono

Japan Synchrotron Radiation Research Institute

Shigeki Owada

RIKEN

Yasumasa Joti

RIKEN SPring-8 Center

Rie Tanaka

RIKEN SPring-8 Center

Eriko Nango

Tohoku University

Fusamichi Akita

Okayama University <https://orcid.org/0000-0003-0537-6157>

Minoru Kubo

University of Hyogo <https://orcid.org/0000-0002-1470-942X>

So Iwata

Kyoto University <https://orcid.org/0000-0003-1735-2937>

Jian-Ren Shen

Okayama University <https://orcid.org/0000-0003-4471-8797>

Michihiro Suga (✉ msuga@okayama-u.ac.jp)

Okayama university <https://orcid.org/0000-0001-8542-5910>

Article

Keywords: photosystem II, PSII, serial femtosecond crystallography, TR-SFX, water-splitting reaction

Posted Date: July 30th, 2020

DOI: <https://doi.org/10.21203/rs.3.rs-41101/v1>

License:  This work is licensed under a Creative Commons Attribution 4.0 International License.

[Read Full License](#)

Abstract

Photosystem II (PSII) catalyzes light-induced water oxidation through an S_i-state cycle, leading to the generation of di-oxygen, protons, and electrons. Pump-probe time-resolved serial femtosecond crystallography (TR-SFX) has been used to capture intermediate states of light-driven enzymatic reactions. In this approach, it is crucial to avoid contamination of light into the samples when analyzing a particular reaction intermediate. Here, we describe a method for determining a proper light condition that avoids light contamination to the PSII microcrystals while minimizing the sample consumption in TR-SFX. With the proper illumination conditions determined, we analyzed the S₂-state structure of PSII at room temperature, revealing the structural changes during the S₁-to-S₂ transition at an ambient temperature. By comparing with the previous studies performed at a low temperature or with a different delay time, we reveal the possible channels for water inlet and proton egress, as well as structural changes important for the water-splitting reaction.

Introduction

Oxygenic photosynthesis converts light energy into chemical energy, thereby sustaining all aerobic life on Earth. The energy-conversion reaction of photosynthesis is carried out by two photosystems (PSs), PSI and PSII, both are large membrane-embedded protein-pigment complexes existing on the thylakoid membranes of plants and various algae. Among these two PSs, PSII uses light energy to extract electrons and protons from water molecules, leading to the oxidation of water and release of dioxygen as a byproduct. This water oxidation reaction is catalyzed by the oxygen-evolving complex (OEC) of PSII and proceeds through a light-driven, five-step S_{*i*}-state cycle (*i*=0-4)¹⁻⁴ (Fig. 1a). In this S_{*i*}-state cycle, S₀ is the ground state, and the OEC progresses to higher S_{*i*}-states upon its oxidation by Y_Z⁺, a tyrosine cation residue generated by P₆₈₀⁺, the photoexcited PSII reaction center P₆₈₀ (Fig. 1b). Dioxygen is released during the S₃ → (S₄) → S₀ transition. The OEC in the S₁ state is dark-stable, and its structure has been determined to have a chemical composition of Mn₄CaO₅^{5,6}. This structure changes to a Mn₄CaO₆-cluster in the highest metastable S₃ state by incorporation of a new oxygen atom (O₆^{7,8} or O_x⁹) near the unique μ-oxo bridge O₅. The interatomic distance between O₆ and O₅ is 1.9-2.0 Å in the S₃ state^{8,9}, which is suitable for an oxyl/oxo type coupling to form dioxygen between them. The detailed mechanism of the water oxidation, however, has not been well understood, in particular with respect to the origin of O₆ and the proton exit pathways.

Since the Mn₄CaO₅ cluster is embedded inside the protein matrix of PSII and covered by a large area of hydrophilic protein regions in the luminal side of the thylakoid membrane, channels for the inlet of substrate waters and egress of the product protons are important for the water-splitting reaction to proceed properly. The high resolution structure of PSII showed multiple hydrogen-bond networks connecting the site of the Mn₄CaO₅ cluster to the luminal surface of PSII complex^{1,5,6} these channels may therefore function to allow water coming into the catalytic site or protons to be transported to the

luminal solution. Four main such channels have been identified; they are designated O1-channel, O4-channel, Cl1-channel, and Cl2-channel (Fig. 1). The O1- and O4-channels are so called because they start from the oxo-bridge O1 and O4 of the Mn_4CaO_5 cluster, respectively, whereas the Cl1- and Cl2-channels are mediated by the Cl1 and Cl2 ions in the vicinity of the Mn_4CaO_5 cluster, respectively. It is not clear which of these channels functions in the water inlet or proton egress, and in the latter case, in which S-state transition.

Pump-probe, time-resolved serial femtosecond X-ray crystallography (TR-SFX) using X-ray free-electron lasers (XFEL) is a powerful method to visualize structural dynamics of light-triggered enzymes¹⁰⁻¹⁵, including PSII in different S_i -states at an ambient temperature^{7, 9, 16}. XFELs are femtosecond pulses of X-ray with billions of times brilliance than that of conventional synchrotron X-rays, thus enabling collection of the diffraction data before the onset of radiation damage¹⁷. For trapping the intermediate S_i -states of PSII with this method, a flow of PSII microcrystals is illuminated by a desired number of pump flashes to generate the higher S_i -states (one, two, or three flashes generate S_2 , S_3 , or S_0 states, respectively), followed by detection with an XFEL pulse with a temporal delay time after the flash illumination. One of the most critical factors for the success of this experiment is the selection of an optimal light excitation condition (intervals, the boundary of excitation region, and power of the excitation laser, etc.) under particular sample delivery conditions (crystal size, flow diameter, flow rate, overall sample consumption, etc.). A generally applicable way to determine a proper light excitation condition is adding a generous safety margin in the sample area to be excited and examining the structural changes by the TR-SFX experiment under a suitable size and power of the pump laser illumination. In the case of enzymes such as PSII that requires multi-flash excitations for the latter S states, however, the application of this method is not straightforward under the continuous sample flow condition, because the sample area that can be used for the excitation and X-ray diffraction data collection must be well aligned spatially and temporally, and a larger separation between two consecutive flashes may make the illuminated sample to escape from the area that can be irradiated by the XFEL pulses. Thus, higher S_i states may not be captured by the TR-SFX method if a too large separation is used between consecutive flashes.

In the present study, we show a method to determine an optimal light illumination condition for successful TR-SFX to analyze the structures of the intermediate S_i -states of PSII. By altering the flash interval distance with a maximum delay time and examining the structural changes that occurs during the S_1 -to- S_2 transition, a boundary of the excitation region was accurately determined. Based on the light illumination conditions determined, we analyzed the PSII structure in the S_2 state at a 2.4-Å resolution. Structural changes were found in the OEC, the O1- and O4-channels, and the Q_B -binding site, providing important insights into the proton transfer and substrate water delivery during the water oxidation reaction.

Determination of a boundary of the excitation region in TR-SFX

We performed TR-SFX as described previously^{7,18}. In this approach, PSII microcrystals were mixed with a grease matrix and ejected from a micro-extrusion injector. The flow of the PSII microcrystals were excited by a single flash to advance the S-state to S₂. Fig. 2a shows a scheme representing the interaction between the pump excitation region and the XFEL pulse in the TR-SFX experiment with a delay time (Δt) of 10 ms at the pump and XFEL repetition rates of 30 Hz. It should be noted that, although the pump beam was focused on the sample stream with a top-hat shape ($\varnothing 250 \mu\text{m}$)¹⁹, the effective excitation region extended upstream due to the pump-light scattering on the stream. Thus, the excitation region is schematically depicted by a triangle in the figure, indicating a gradual decrease in the pump photon density along the sample stream. When a flow rate is not fast enough for the sample exchange, the pump excitation region interacts with the next pump-XFEL pulse pair (Fig. 2b). To avoid such erroneous light-contamination, we here designed a test experiment with Δt of minus 50 ns, where XFEL pulses were delivered to the microcrystals about 100 ms (99.99995 ms) after the pump illumination (Fig. 2c). On this negative Δt condition, if the flow rate is slow, the microcrystals would be illuminated partially by the preceding flash, resulting in “one-flash” illumination (Fig. 2d). However, at a sufficiently fast flow rate, the microcrystals at the position of the XFEL shot will escape from the preceding flash illumination (Fig. 2e), resulting in a “dark dataset”. Accordingly, we can check light-contamination, including an effect of pump light scattering on the sample stream, under the given experimental conditions (pump-illumination size and intensity, sample flow rate, etc).

Four diffraction datasets were collected at different flow rates of 4.9 $\mu\text{l}/\text{m}$, 7.3 $\mu\text{l}/\text{m}$, 8.5 $\mu\text{l}/\text{m}$ and 9.8 $\mu\text{l}/\text{m}$ (corresponding to 2.0 times, 3.0 times, 3.5 times, and 4.0 times of that for the dark datasets), respectively. In addition to these four datasets, we collected two independent dark datasets from different preparations (Dark1 for the light-illuminated, flow rate 4.9 $\mu\text{l}/\text{m}$ and 7.3 $\mu\text{l}/\text{m}$ experiments, and Dark2 for the light-illuminated, flow rate 8.5 $\mu\text{l}/\text{m}$ and 9.8 $\mu\text{l}/\text{m}$ experiments) at a flow rate of 2.5 $\mu\text{l}/\text{m}$, and a light dataset with Δt of 10 ms at a flow rate of 9.8 $\mu\text{l}/\text{m}$. All datasets were processed at 2.35 to 2.40-Å resolutions (Table 1).

We evaluated the boundary of the excitation region as follows (Methods). Isomorphous difference *Fourier* maps between the “light”-illuminated and dark datasets were calculated with the phases obtained by the refinement, which showed a negative peak covering W665, the second water molecule from O4 in the O4-channel (Fig. 1c, d). Since a similar negative peak has been observed in the previous studies, indicating that W665 becomes highly disordered during the S₁-to-S₂ transition⁷⁻⁹, we take the height of the *Fourier* difference peak of W665 as an indicator for the light-induced structural changes. The F_{obs} (-50 ns, “light” at 4.9 $\mu\text{l}/\text{m}$) minus F_{obs} (dark) difference *Fourier* map showed a sharp peak height of -6.4σ at the position of W665 (Fig. 3a). This peak height is lower than that observed with a delay time of 10 ms after the excitation flash (Fig. 3e), but apparently higher than the maximum noise level (Fig. 3f), suggesting that at this flow rate, the microcrystals at the target position of the XFEL shot has been excited by the preceding flash illumination. Thus, the flow rate of 4.9 $\mu\text{l}/\text{m}$ is too slow to avoid the light-contamination by the preceding flash in the excitation region. The average height of the light-minus-dark *Fourier* difference peak of W665 in two non-crystallographic symmetry-related PSII monomers was reduced when the flow

rate was increased (Fig. 3b-d), and reached to a level not visible in the difference map contoured at $\pm 4.0\sigma$ at the flow rate of $9.8 \mu\text{l}/\text{m}$ (Fig. 3d), which is also well below the maximum noise level (Fig. 3f). This indicates that at the flow rate of $9.8 \mu\text{l}/\text{m}$, no apparent light-minus-dark *Fourier* difference peak was observed. Therefore, we concluded that the flow rate of $9.8 \mu\text{l}/\text{m}$ gives rise to no light-contamination at the position of the XFEL shot. Therefore, we collected the light-illuminated dataset with a Δt of 10 ms after the flash illumination at this flow rate to analyze the PSII structure in the S_2 state.

Structural determination of PSII in the S_2 state

The F_{obs} (10 ms, light, $9.8 \mu\text{l}/\text{m}$) minus F_{obs} (dark) isomorphous difference *Fourier* map showed a strong signal with a peak height above -11.3σ at the position of W665, suggesting that the microcrystals were successfully excited to progress to the S_2 state (Fig. 3e, f). Many peaks can be seen in the *Fourier* difference map when we decrease the contour level below $\pm 3\sigma$; thus we consider that the average noise level is at around $\pm 3\sigma$, and peaks above $\pm 3\sigma$ may represent real structural changes induced by one-flash illumination. Most of the peaks that are related to the light-induced structural changes were above $\pm 4.5\sigma$ and distributed around the electron transfer chain (the OEC, bicarbonate (BCT), non-heme iron, and Q_B), and were observed similarly in both PSII monomers. However, some weaker peaks at around $\pm 4\sigma$ were found at one side of the monomer-monomer interface (Fig. 3g). These weaker peaks may not be related with the light-induced structural changes, and possibly induced by a relatively low isomorphism between the two datasets. These may arise from differences in the batches of samples used, since it was difficult to control the sample purification conditions and sample states, such as dehydration of the crystals, to an entirely uniform one. Nevertheless, we were able to distinguish the essential, light-induced structural changes during the catalytic reaction from the ones associated with the differences in the samples employed based on their peak intensities.

We refined the 10 ms light dataset as a mixture model consisting of 70% S_2 state and 30% S_1 state for the Mn_4CaO_5 -cluster and the nearby residues (Method). This gives rise to equivalent values of the temperature factors between the two equivalent atoms in the multiple model, and this population of S_2 and S_1 -states after one-flash illumination is similar to the efficiencies of the S_1 -state transition estimated by the *Fourier* transform infrared spectroscopy^{7,20}. The OEC structures in the S_1 and S_2 states determined in the present study are similar to those reported in the previous studies^{8,9}. The OEC structure in the S_2 state was in the open-cubane form, in which the right side of the O5 is open, giving rise to the five-coordinate trigonal bipyramidal coordination of Mn1. All changes in the Mn-Mn and Mn-Ca distances during the S_1 -to- S_2 transition were less than the error range of the coordinates at the current resolution (Fig. 4). However, the changes found in the isomorphous difference *Fourier* map, such as the shorting of Mn3-Mn4 and elongations of Mn1-Mn3, Mn3-Ca, and Mn4-Ca, were consistent with the previous study with the diffraction data collected at 100 K for the room temperature-trapped S_2 -state⁸ (Fig. 4 and Table 2). In association with the movements of these manganese atoms, some ligand residues of the OEC (D1-E189, E333, D342, A344, and CP43-E354) also moved slightly (Fig. 5b).

Structural changes in the O4 and O1 channels

Among the four channels, the O4-channel has been suggested to function as the pathway of proton release during the S_0 -to- S_1 transition based on theoretical calculations²¹. On the other hand, other groups argued that it serves as the source of substrate water by a “pivot” or “carousel” mechanism in the transition of S_2 -to- S_3 ²²⁻²⁴. As described above, upon transition to the S_2 state, W665 in the O4-channel became highly disordered. This is accompanied by slight shifts of the nearby residues D1-D61 and CP43-E354 toward the position of W665, resulting in a narrowing of the space that has been occupied by W665 (Figs. 3e and 5b). A water cluster (W546, W548, W612, W606, and W806) leading to the luminal surface in the O4-channel also shifted their positions during the S_1 -to- S_2 transition, and the shift of W548 induced structural changes of its H-bond partners R334 and N335 (Fig. 5a). These changes in the O4-channel were similar to the previous study analyzed at the cryogenic temperature⁸. However, another water molecule, W757, connected to W548 and W606 in this channel, was found to become disordered in the S_1 -to- S_2 transition at the cryogenic temperature⁸, but this water molecule was not detected in both the S_1 and S_2 structures in the present study, presumably due to its peripheral location and thus weaker association within the channel, resulting in a higher mobility at room temperature at which the TR-SFX experiments were conducted in the present study.

Another noticeable change observed near the OEC was a negative peak of -7.4σ covering W601, the H-bond donor to O1 and one of the members of a diamond-shaped water cluster in the O1-channel (Fig. 5b). This indicates that W601 became disordered in the S_1 -to- S_2 transition. This change was not found in our previous study performed at the cryogenic temperature⁸. Another SFX study at ambient temperature by Kern et al. reported the shifts of three water molecules W601, W547, and W536 (W26, W27, and W30)⁹ of the diamond-shaped water cluster. In contrast, our previous fixed-target SFX study at cryogenic temperature reported W571, a water molecule found at a cryogenic temperature only, became disordered instead of W601⁸. These differences indicate a high mobility of the water molecules in the O1-channel during the S_1 -to- S_2 transition. Such an increase of the mobility during the S_1 -to- S_2 transition at room temperature may be necessary to allow incorporation of the substrate water molecule(s) into the OEC during the S_2 -to- S_3 transition, which in turn suggests that the O1-channel may be responsible for the substrate water to enter into the reaction site.

Q_B and the non-heme iron site

After one flash illumination, the second bound quinone electron acceptor Q_B undergoes reduction and protonation to form a stable plastosemiquinone intermediate Q_BH^\cdot . The isomorphous difference *Fourier* map showed a positive peak covering the Q_B head and a pair of positive and negative peaks over the Q_B tail, suggesting its slight movement during the S_1 -to- S_2 transition (Fig. 5c). The B-factor of the Q_B head was decreased from 121 \AA^2 in the S_1 -state to 103 \AA^2 in the S_2 -state, and the H-bond length between the head of Q_B and S264 was also changed from 2.92 \AA in the S_1 -state to 2.77 \AA in the S_2 -state, indicating a

tighter binding of Q_BH^+ to S264. Thus, the first protonation of Q_B may occur at this site. This notion is consistent with the theoretical calculation that the first proton transfer from S264 to Q_B is an energetically downhill process, whereas it is an uphill one from H215 to Q_B ²⁵. Several pairs of positive and negative peaks were also found around the H-bond network formed by the bicarbonate (BCT), D1-Y246, D1-E244, D2-K264, and D2-E242, and BCT moved 0.39 Å away from the non-heme iron (Fig. 5c). These changes may be related to the reduction of the non-heme iron or proton uptake after one flash illumination, which in turn suggests that these residues form part of the proton inlet channel for the protonation of Q_B .[□]

Discussions

For the success of the pump-probe TR-SFX experiments to analyze intermediate structures of enzymes using light as the pump to initiate the reaction, it is critical to find an optimal light excitation condition with an optimal sample delivery system. These conditions vary considerably depending on the sample of interests as well as the setup of the pump-probe SFX system. Under optimal conditions, one can save a large amount of the valuable protein samples as well as the XFEL beamtime to obtain structures of the targeted intermediate states. In the present study, we showed a method to determine a boundary excited by the pump by altering the flow rate of the microcrystals and evaluating the resulted light-induced structural changes of PSII. With the optimal conditions obtained, we analyzed the structure of PSII in the S_2 state at room temperature by the TR-SFX method. This method can apply to other samples whose catalytic reaction are triggered by light, by using systems which deliver microcrystals in a continuous flow. Importantly, this method also provides a suitable light condition for samples, such as PSII, that require successive flash excitations for its catalytic cycle.

The PSII structures in the S_1 and S_2 states, as well as the isomorphous difference *Fourier* map obtained in the present study, revealed the light-induced structural changes localized at the OEC, Q_B site, and water molecules in the O1 and O4 channels. Comparison of the changes observed at the ambient temperature with a Δt of 10 ms obtained in the present study, with the previous study where the S_2 -state was trapped cryogenically with a Δt of around one s and the diffraction data collected at a low temperature⁸, as well as that carried out at the ambient temperature with a Δt of 200 ms⁹, shows an overall tendency of the structural changes. The changes found in the OEC were identical regardless of the ambient/cryogenic temperatures or the different Δt , suggesting the stability and the long lifetime of the catalytic center in the S_2 -state. By contrast, the changes found in some amino acid residues and water molecules differ substantially either depending on the temperatures or Δt , reflecting a rather large mobility of the protein environment. This tendency is apparent in the Q_B site, in which the quinone changes its redox forms during the catalytic cycle. The changes in the Q_B site were larger with the Δt of 10 ms but smaller with the Δt of 200 ms⁹ and further diminished at the Δt of around one s⁸.

Comparisons of the structural changes in the O1 and O4-channels with the previous crystallographic studies^{8,9} also reveal the characteristic properties of the water molecules. W665, the second water from

O4 in the O4-channel, became highly mobile in the S_1 -to- S_2 transition, which is consistent with the previous studies. The disorder of W665 breaks the H-bond network in the O4-channel in the S_2 -state. In our initial report of the disorder of W665 in the S_2 -state, we proposed that proton transfer may occur in the O4-channel in the S_1 -to- S_2 transition⁸. The changes observed in the O4-channel were similar to the theoretical calculation that reported a proton release in the channel in the S_0 -to- S_1 transition²¹. However, FTIR studies on D1-S169A mutant, which perturbs the interaction of a water molecule hydrogen-bonded with O4, showed only minor effects on the efficiencies or kinetics of the S_i -state transitions^{26, 27}. In contrast, the S_2 -state multiline EPR spectrum of the D1-S169A mutant differs significantly from that of wild-type²⁷. A further theoretical study on the O4-channel showed that the removal of water molecules in the O4-channel results in a decrease in the S_2/S_1 redox potential by ~ 80 mV²⁸. Therefore, the weakened H-bond network due to the increased mobility of W665 may be necessary for the decrease in the redox potential to facilitate the S_1 -to- S_2 transition.

In contrast to the changes observed in the O4-channel, the changes in the water molecules of the O1-channel differ between the present and previous studies. W601, the H-bond donor to O1, became disordered in the present study at a Δt of 10 ms, and two additional water molecules W547 and W536 (W26, W27, and W29)⁹ became disordered at a Δt of 200 ms. However, instead of these water molecules, W571 became disordered in the study with a Δt of around one s at the cryogenic temperature⁸. Because the O1-channel is a broad channel where water molecules are the major component of the H-bond network, substrate water molecules likely propagate through the waters in the O1-channel. Increasing the mobility of waters in this channel may be of benefit in driving the incorporation of the substrate water into the catalytic site in the following S_3 state.

Fig. 6 summarizes the structural changes regarding the water molecules in the O1 and O4-channels observed in the present study. In the S_1 -to- S_2 transition, W665 in the O4-channel becomes highly mobile, disconnecting the 15-Å long water chain starting from O4-W567. W665 remains disordered in the S_3 state but becomes re-ordered beyond the S_3 state^{8, 9}. W601 in the O1-channel also becomes disordered in the S_1 -to- S_2 transition. The mobility of W601 is propagated to W547, W536, and W571 through the H-bond network in the O1-channel. D1-E189, the only monodentate carboxyl ligand of the OEC, flips by 0.5-Å in the following S_2 -to- S_3 transition, leading to the broadening of the O1-channel, thereby further increases the mobility of water molecules there⁷⁻⁹. The flipping of D1-E189 makes a space in the vicinity of O5 to allow the insertion of the additional water (oxygen) O6 in the subsequent S_2 -to- S_3 transition. This suggests that waters in the O1-channel may be the source for O6. Dioxygen is then likely formed between O5 and O6, or between O5 and another water molecule, by an oxyl/oxo coupling mechanism, and in the latter case, O6 refills the empty substrate site. The changes of waters in the O1-channel support the mechanism of water delivery from the Ca side^{8, 29, 30}, rather than the O4-channel²²⁻²⁴. Further structural analysis will be required to reveal how the OEC incorporates those waters in the O1-channel and how protons egress during the subsequent S-state transitions.

Methods

Preparation and crystallization of photosystem II.

Highly active dimeric PSII core complexes were purified from the thermophilic cyanobacterium *Thermosynechococcus vulcanus* cells and crystallized as described previously^{6,7}. The microcrystals grew to a maximum size of 100 μm and showed a good quality in diffraction as well as a high efficiency in the progress of the S_F -state cycle. Prior to the TR-SFX experiments, the microcrystals were pre-flashed by a Nd:YAG laser at 532 nm with a diameter of 7 mm at an energy of around 52 mJ/cm^2 , to oxidize the tyrosine D residue (D2-Y160) and decrease the contamination of the S_0 state. Then the microcrystals were dehydrated with a buffer containing 20% glycerol, 10% PEG 1,450, 10% PEG 5,000 MME, 2% dimethyl sulfoxide, and 10 mM potassium ferricyanide in the crystallization buffer by stepwise replacement of the solution, which took around two hours. Following the dehydration, the crystals were mixed with a silicon grease¹⁸ and used for the TR-SFX experiments. All the procedures, including purification, crystallization, pre-flash illumination, dehydration, and mixing with the grease matrix, were performed in the dark or under dim green light.

Diffraction experiments at SACLA-XFEL.

The PSII crystals mixed with the grease matrix were loaded into an injector³¹ with a nozzle diameter of 140 μm and set in a pump-probe system based on Diverse Application Platform for Hard X-ray Diffraction in SPring-8 Angstrom Compact Free Electron Laser (SACLA) (DAPHNIS)^{19,32}. The flow rates were set as follows: 2.5 $\mu\text{l}/\text{m}$ for the dark datasets; 4.9 $\mu\text{l}/\text{m}$, 7.3 $\mu\text{l}/\text{m}$, 8.5 $\mu\text{l}/\text{m}$, and 9.8 $\mu\text{l}/\text{m}$, for each “light” dataset at a delay time of -50 ns; 9.8 $\mu\text{l}/\text{m}$ for the light dataset at a delay time of 10 ms. As the pump laser, a 532 nm pulse from Nd:YAG laser source (Minilite-I, Continuum) with a repetition of 10 Hz was split into two beams, and each beam was focused on the microcrystals from two different directions with an angle of 160° to ensure sufficient excitation⁷. The pump focal diameter was set to 240 μm at the targeted sample position, and its energy was 42 mJ/cm^2 from each direction. Diffraction images were collected using femtosecond X-ray pulses from SACLA at BL3 with the following pulse parameters: pulse duration, 2–10 fs; X-ray energy, 7 keV; energy bandwidth, 0.5% (FWHM); pulse flux, $\sim 7 \times 10^{10}$ photons per pulse; beam size 3.0 μm (H) \times 3.0 μm (W); repetition rate, 30 Hz. The XFEL pulses were provided to the pump focal center either before 50 ns of the pump laser pulse for the “light” datasets at different flow rates, or 106 μm downstream from the pump focal center after 10 ms of the pump laser pulse for the light dataset that transform the S state fully to the S_2 state. Diffraction images were recorded by a multiport CCD detector. Because the excitation laser pulses were provided at 10 Hz and the XFEL pulses had a repetition rate of 30 Hz, each “pump-on” images were recorded at 10 Hz for the “light” datasets, whereas the diffraction data for the dark dataset were recorded at 30 Hz in a separate run.

Data processing.

The diffraction data collected at SACLA was monitored by the program *cheetah*^{33,34}, and the diffraction images passing through the “filter” with pre-defined thresholds of diffraction spot numbers (recorded as “hit”) were used for the subsequent processing. Indexing, integration, scaling, and merging of the images were carried out by programs in the *cctbx.xfel* suite^{35,36,37}. The diffraction images were indexed and integrated by the program *dials.stills_process* using the geometry of the detector and a camera distance refined by the program *cspad.cbf_metrology*. The unit cell parameters ($a=126.28$, $b=232.13$, $c=289.03$, and $\alpha=\beta=\gamma=90^\circ$), which was originally determined by the program *CrystFEL*³⁸ was provided during the indexing process. The number of indexed images for each dataset were as follows: 96,459 for Dark1; 41,071 for Dark2; 18,216 for -50 ns, “light”, 4.9 $\mu\text{l/m}$; 13,858 for -50 ns, “light”, 7.3 $\mu\text{l/m}$; 20,449 for -50 ns, “light”, 8.5 $\mu\text{l/m}$; 22,419 for -50 ns, “light”, 9.8 $\mu\text{l/m}$; 17,247 for 10 ms, light, 9.8 $\mu\text{l/m}$, datasets (Table 1). Integrated images were merged by the program *cxi.merge* with the post refinement rs2 algorithm, and a filter based on the value of $I/\sigma(I)$ was not applied to include weak signals at high resolution. Dark1 or Dark2 was used as the reference model in the processing of the “light” datasets from the same purification. All datasets are processed to 2.35-2.40 Å resolutions based on the criteria of $CC_{1/2}$ larger than 50%. The R_{iso} values between the datasets were 0.073 to 0.100 in the same sample batch, and 0.095 to 0.112 between the different sample batches. Because different sample batches gave a slightly higher R_{iso} between the different datasets and because lower R_{iso} was crucial to detect meaningful structural changes based on the isomorphous difference *Fourier* map, we collected the two different dark datasets (Dark1 and Dark2) independently for the different sample bathes used.

Model building and map calculation

The initial phase of the dark dataset was obtained by molecular replacement with the program *Phaser-MR* in the CCP4 package³⁹, using the previous PSII structure at room temperature (PDB code: 5ws5)⁷ as the search model. Then, an initial rigid-body refinement, followed by refinement of coordinates, B factors, and TLS, was performed by the program, *Phenix*^{40,41} combined with manual modifications with the program *Coot*⁴². The restraints used here were the same as those used previously^{7,8}. The final R_{factor} and R_{free} were 0.170 and 0.214 for the Dark1 dataset, and 0.179 and 0.219 for the Dark2 dataset (Table 1). The phases from the refined model of dark1 or dark2 were used to calculate the isomorphous difference *Fourier* maps between dark and each -50 ns, “light”, datasets or 10 ms, light, dataset. Sharp peaks in the isomorphous difference *Fourier* maps were localized around the regions of the OEC, Q_B , non-heme iron, and those regions were built as a mixture of dominant S_2 state and minor S_1 state based on the transition efficiency of the PSII microcrystals²⁰. We first refined coordinates of dominant S_2 state only with fixed B-factors. Then we refined the B-factors of atoms in the regions mentioned above that show structural changes during the S_1 -to- S_2 transition by assuming the populations of the S_2 and S_1 states at (0.9, 0.1), (0.8, 0.2), (0.7, 0.3) and (0.6, 0.4), and found that the residual electron densities and B-factors after the refinement was reasonable with the population of S_2 and S_1 states of 0.7 and 0.3, respectively. Thus, this population was used to refine the final structure in the S_2 state. The statistics for structural refinement were provided in Table 1.

Declarations

Data availability

The structure factors and atomic coordinates have been deposited in the Protein Data Bank (PDB) with accession numbers 7CJI and 7CJJ for the dark2 and 10 ms, light datasets, respectively. All other data associated with this manuscript are available from the authors on a reasonable request.

Acknowledgments

We thank T. Nakano and S. Goda for growing and harvesting the cyanobacterial cells. This work was supported by JSPS KAKENHI Grants JP17H05884, JP20H05446, JP20H03226 (M. Suga), JP17H06434 (J.-R. S.), JP19H05784 (M. K.), JP19H05781 (E. N.), and JST, PREST grants JPMJPR18G8 (M. Suga), JPMJPR16P1 (F. A.). S.I.

supported by Platform Project for Supporting Drug Discovery and Life Science Research (Basis for Supporting Innovative Drug Discovery and Life Science Research (BINDS)) from Japan Agency for Medical Research and Development (AMED). The XFEL experiments were performed at beamlines 2 and 3 of SACLA with the approval of the Japan Synchrotron Radiation Research Institute (JASRI) (proposals 2016A8033, 2016B8066, 2017A8041, 2017B8025, 2018A8037, and 2018B8029) and we thank the staff at SACLA for their help. We also acknowledge the computational support from SACLA HPC system and Mini-K supercomputer system.

Author contributions

J.-R. S. conceived the project; M. Suga, M. K., E. N., and J.-R. S. designed the experiments; Y. N., S. Y., and S. K. C. purified and crystalized PSII; M. Suga, H. L., Y. N., M. Sugah., S. Y., S. K. C., T. Y., Y. U., T. Ma., M. Suz., T. Mo., H. N., Y. M., R. T., F. A., and J.-R. S. participated in the data collection. M. K., T. No., and T. K. designed the pump excitation scheme; K. T., S. O., and Y. J. operated beamline. T. Na., and S. I. Developed the data evaluation and hit finding programs for TR-SFX; T. Na. adapted DIALS for MPCCD datasets. H. L., T. Y., and M. Suga analyzed the X-ray diffraction; L. H., M. Suga, and J.-R. S. wrote the paper with inputs from all authors.

References

1. Shen JR. The Structure of Photosystem II and the Mechanism of Water Oxidation in Photosynthesis. *Annual review of plant biology* 66, 23–48 (2015).
2. Cox N, Pantazis DA, Neese F, Lubitz W. Biological water oxidation. *Accounts of chemical research* 46, 1588–1596 (2013).
3. Yano J, Yachandra V. Mn₄Ca cluster in photosynthesis: where and how water is oxidized to dioxygen. *Chem Rev* 114, 4175–4205 (2014).

4. Kok BF, B.; McGloin, M.. Cooperation of charges in photosynthetic O₂ evolution-I. A linear four step mechanism. *Photochem Photobiol* 11, 457–475 (1970).
5. Suga M, *et al.* Native structure of photosystem II at 1.95 angstrom resolution viewed by femtosecond X-ray pulses. *Nature* 517, 99-U265 (2015).
6. Umena Y, Kawakami K, Shen JR, Kamiya N. Crystal structure of oxygen-evolving photosystem II at a resolution of 1.9 Å. *Nature* 473, 55–60 (2011).
7. Suga M, *et al.* Light-induced structural changes and the site of O = O bond formation in PSII caught by XFEL. *Nature*, (2017).
8. Suga M, *et al.* An oxyl/oxo mechanism for oxygen-oxygen coupling in PSII revealed by an x-ray free-electron laser. *Science* 366, 334–338 (2019).
9. Kern J, *et al.* Structures of the intermediates of Kok's photosynthetic water oxidation clock. *Nature* 563, 421–425 (2018).
10. Nango E, *et al.* A three-dimensional movie of structural changes in bacteriorhodopsin. *Science* 354, 1552–1557 (2016).
11. Barends TR, *et al.* Direct observation of ultrafast collective motions in CO myoglobin upon ligand dissociation. *Science* 350, 445–450 (2015).
12. Pande K, *et al.* Femtosecond structural dynamics drives the trans/cis isomerization in photoactive yellow protein. *Science* 352, 725–729 (2016).
13. Tenboer J, *et al.* Time-resolved serial crystallography captures high-resolution intermediates of photoactive yellow protein. *Science* 346, 1242–1246 (2014).
14. Nogly P, *et al.* Retinal isomerization in bacteriorhodopsin captured by a femtosecond x-ray laser. *Science* 361, (2018).
15. Suga M, Shimada A, Akita F, Shen JR, Toshi T, Sugimoto H. Time-resolved studies of metalloproteins using X-ray free electron laser radiation at SACLA. *Biochim Biophys Acta Gen Subj* 1864, 129466 (2020).
16. Kupitz C, *et al.* Serial time-resolved crystallography of photosystem II using a femtosecond X-ray laser. *Nature*, (2014).
17. Neutze R, Wouts R, van der Spoel D, Weckert E, Hajdu J. Potential for biomolecular imaging with femtosecond X-ray pulses. *Nature* 406, 752–757 (2000).
18. Sugahara M, *et al.* Grease matrix as a versatile carrier of proteins for serial crystallography. *Nature methods* 12, 61–63 (2015).
19. Kubo M, *et al.* Nanosecond pump-probe device for time-resolved serial femtosecond crystallography developed at SACLA. *Journal of synchrotron radiation* 24, 1086–1091 (2017).
20. Kato Y, *et al.* Fourier Transform Infrared Analysis of the S-State Cycle of Water Oxidation in the Microcrystals of Photosystem II. *J Phys Chem Lett*, (2018).
21. Saito K, William Rutherford A, Ishikita H. Energetics of proton release on the first oxidation step in the water-oxidizing enzyme. *Nature communications* 6, 8488 (2015).

22. Wang J, Askerka M, Brudvig GW, Batista VS. Crystallographic Data Support the Carousel Mechanism of Water Supply to the Oxygen-Evolving Complex of Photosystem II. *ACS Energy Letters*, 2299–2306 (2017).
23. Retegan M, *et al.* A five-coordinate Mn(IV) intermediate in biological water oxidation: spectroscopic signature and a pivot mechanism for water binding. *Chem Sci* 7, 72–84 (2016).
24. Kawashima K, Takaoka T, Kimura H, Saito K, Ishikita H. O₂ evolution and recovery of the water-oxidizing enzyme. *Nature communications* 9, 1247 (2018).
25. Saito K, Rutherford AW, Ishikita H. Mechanism of proton-coupled quinone reduction in Photosystem II. *Proceedings of the National Academy of Sciences of the United States of America* 110, 954–959 (2013).
26. Shimada Y, Kitajima-Ihara T, Nagao R, Noguchi T. Role of the O₄ Channel in Photosynthetic Water Oxidation as Revealed by Fourier Transform Infrared Difference and Time-Resolved Infrared Analysis of the D1-S169A Mutant. *The journal of physical chemistry B* 124, 1470–1480 (2020).
27. Ghosh I, *et al.* D1-S169A Substitution of Photosystem II Perturbs Water Oxidation. *Biochemistry* 58, 1379–1387 (2019).
28. Mandal M, Kawashima K, Saito K, Ishikita H. Redox Potential of the Oxygen-Evolving Complex in the Electron Transfer Cascade of Photosystem II. *Journal of Physical Chemistry Letters* 11, 249–255 (2020).
29. Kim CJ, Debus RJ. One of the Substrate Waters for O₂ Formation in Photosystem II Is Provided by the Water-Splitting Mn₄CaO₅ Cluster's Ca(2+) Ion. *Biochemistry* 58, 3185–3192 (2019).
30. Sakamoto H, Shimizu T, Nagao R, Noguchi T. Monitoring the Reaction Process During the S₂ → S₃ Transition in Photosynthetic Water Oxidation Using Time-Resolved Infrared Spectroscopy. *Journal of the American Chemical Society* 139, 2022–2029 (2017).
31. Shimazu Y, *et al.* High-viscosity sample-injection device for serial femtosecond crystallography at atmospheric pressure. *Journal of applied crystallography* 52, 1280–1288 (2019).
32. Tono K, *et al.* Diverse application platform for hard X-ray diffraction in SACLA (DAPHNIS): application to serial protein crystallography using an X-ray free-electron laser. *Journal of synchrotron radiation* 22, 532–537 (2015).
33. Barty A, *et al.* Cheetah: software for high-throughput reduction and analysis of serial femtosecond X-ray diffraction data. *J Appl Crystallogr* 47, 1118–1131 (2014).
34. Nakane T, *et al.* Data processing pipeline for serial femtosecond crystallography at SACLA. *Journal of Applied Crystallography* 49, 1035–1041 (2016).
35. Sauter NK, Hattne J, Grosse-Kunstleve RW, Echols N. New Python-based methods for data processing. *Acta Crystallogr D Biol Crystallogr* 69, 1274–1282 (2013).
36. Sauter NK. XFEL diffraction: developing processing methods to optimize data quality. *J Synchrotron Radiat* 22, 239–248 (2015).

37. Waterman DG, *et al.* Diffraction-geometry refinement in the DIALS framework. *Acta Crystallogr D Struct Biol* 72, 558–575 (2016).
38. White TA, *et al.* CrystFEL: a software suite for snapshot serial crystallography. *Journal of applied crystallography* 45, 335–341 (2012).
39. Collaborative Computational Project N. The CCP4 suite: programs for protein crystallography. *Acta crystallographica Section D, Biological crystallography* 50, 760–763 (1994).
40. Adams PD, *et al.* PHENIX: a comprehensive Python-based system for macromolecular structure solution. *Acta crystallographica Section D, Biological crystallography* 66, 213–221 (2010).
41. Afonine PV, *et al.* Towards automated crystallographic structure refinement with phenix.refine. *Acta Crystallogr D Biol Crystallogr* 68, 352–367 (2012).
42. Emsley P, Cowtan K. Coot: model-building tools for molecular graphics. *Acta crystallographica Section D, Biological crystallography* 60, 2126–2132 (2004).

Tables

Table 1 Statistics for data collection and structural refinement.

Data name	Dark1	Dark2	-50 ns, "light", 4.9 $\mu\text{l}/\text{m}$	-50 ns, "light", 7.3 $\mu\text{l}/\text{m}$	-50 ns, "light", 8.5 $\mu\text{l}/\text{m}$	-50 ns, "light", 9.8 $\mu\text{l}/\text{m}$	10 ms, light, 9.8 $\mu\text{l}/\text{m}$
Data collection							
Flow rate ($\mu\text{l}/\text{m}$)	2.5	2.5	4.9	7.3	8.5	9.8	9.8
No. of indexed images	96,459	41,071	18,216	13,858	20,449	22,419	17,247
Space group	$P2_12_12_1$						
Unit cell (\AA)	a=126.1, b=231.7, c=288.3	a=126.0, b=231.7, c=288.3	a=125.8, b=231.5, c=288.2	a=126.0, b=231.6, c=288.2	a=125.7, b=231.6, c=288.4	a=125.6, b=231.7, c=288.5	a=125.7, b=231.5, c=288.3
Resolution (\AA)	40 - 2.40	40 - 2.35	40 - 2.40	40 - 2.40	40 - 2.40	40 - 2.40	40 - 2.40
Highest shell (\AA)	2.49 - 2.40	2.43 - 2.35	2.49 - 2.40	2.49 - 2.40	2.49 - 2.40	2.49 - 2.40	2.49 - 2.40
No. of unique reflections	351,161	351,162	329,839	329,852	329,843	329,840	329,844
Completeness (%)	100.0	100	100	100	100	100	100
Multiplicity	913 (629)	494 (339)	159 (109)	111 (76)	249 (172)	271 (187)	235 (162)
$R_{\text{split}}^{\ddagger}$ (%)	3.9 (38.0)	5.7 (56.5)	8.1 (60.7)	10.8 (76.6)	6.7 (53.3)	7.3 (56.4)	8.4 (63.8)
$\text{CC}_{1/2}^{\S}$	0.999 (0.78)	0.999 (0.60)	0.996 (0.610)	0.994 (0.452)	0.998 (0.706)	0.997 (0.643)	0.997 (0.540)
mean $I/\sigma(I)$	74.1 (2.8)	56.8 (2.0)	36.9 (1.8)	27.1 (1.4)	43.1 (2.1)	40.2 (2.0)	37.0 (1.8)
Refinement							
$R_{\text{work}} / R_{\text{free}}$ (%)	0.170 / 0.215	0.163 / 0.221					0.166 / 0.233
Wilson B (\AA^2)	50.0	52.0					50.8
Average B-factor (\AA^2)	64.0	68.6					63.8
Protein	62.0	66.4					63.6
OEC	47.3	49.9					47.5

Water	63.0	68.9	65.6
RMSD bond length (Å)	0.008	0.008	0.009
RMSD bond angle (deg.)	1.292	1.187	1.306
Ramachandran (%)			
Favored	98.00	97.56	97.39
Allowed	1.92	2.25	2.38
Outliers	0.08	0.19	0.23
PDB code	NA	7CJI	7CJJ

Values in parenthesis are those of the highest resolution shell.

Table 2. Interatomic distances of the OEC and their comparisons between different structures.

	The present study (RT)		Suga et al. (100 K) ⁸		Kern et al. (RT) ⁹	
	S ₁	S ₂	S ₁	S ₂	S ₁	S ₂
Mn1-Mn2	2.65	2.63	2.60	2.68	2.78	2.81
Mn1-Mn3	3.16	3.19	3.16	3.21	3.25	3.26
Mn1-Mn4	4.92	4.90	4.97	4.90	4.86	4.86
Mn2-Mn3	2.77	2.72	2.72	2.75	2.85	2.84
Mn2-Mn4	5.27	5.19	5.27	5.20	5.21	5.24
Mn3-Mn4	2.83	2.78	2.89	2.76	2.74	2.74
Mn1-Ca	3.51	3.53	3.61	3.51	3.43	3.42
Mn2-Ca	3.43	3.44	3.42	3.40	3.38	3.41
Mn3-Ca	3.46	3.59	3.40	3.46	3.51	3.52
Mn4-Ca	3.88	4.04	3.76	3.90	3.83	3.90

Figures

Fig. 1

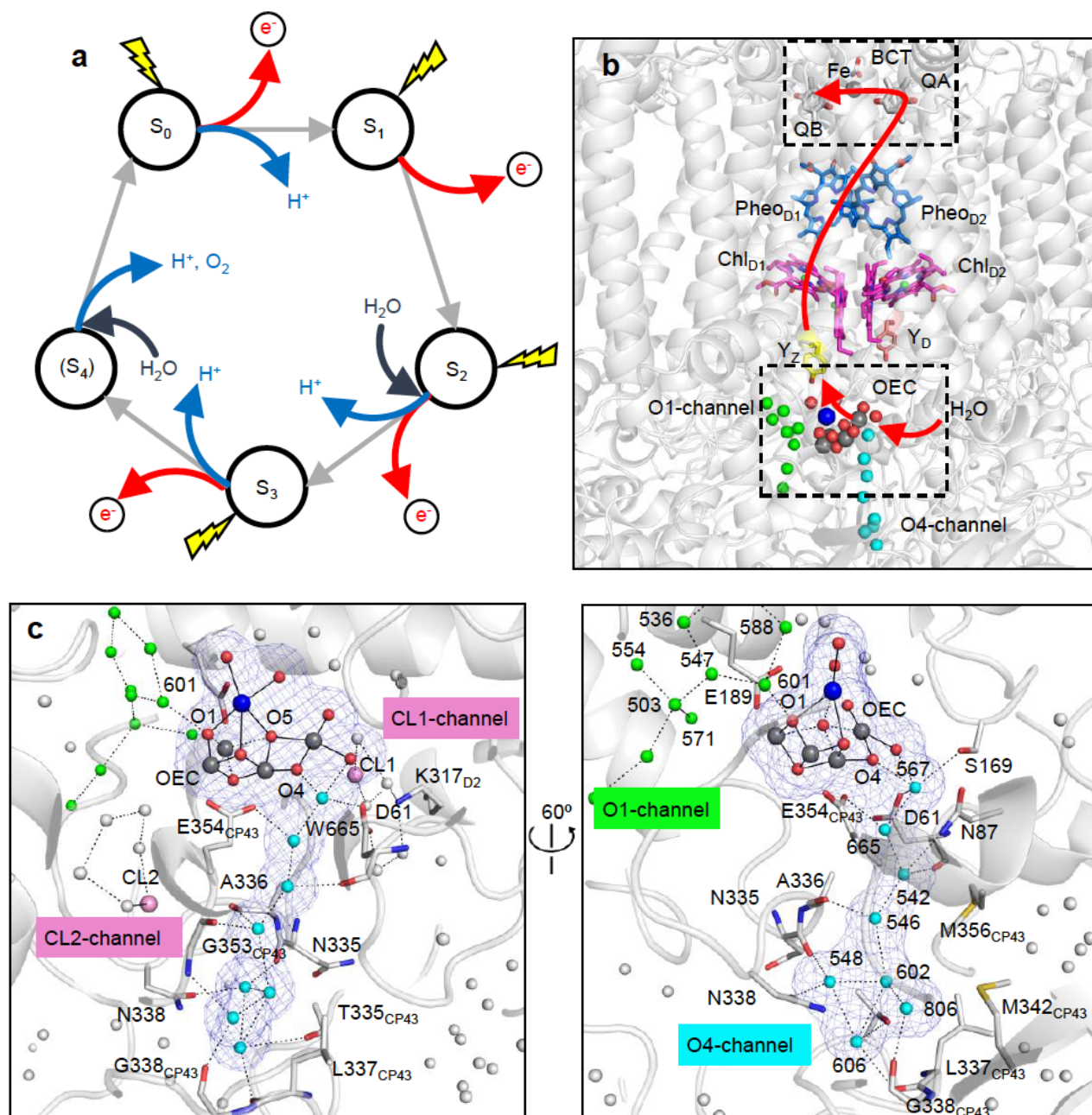


Figure 1

Si-state cycle for the water oxidation reaction and water channels in PSII. a Si-state cycle of the water-oxidation reaction of OEC. b Electron transfer chain of PSII. A flow of electron is indicated by a red line, and the regions around the OEC, QB and the non-heme iron are boxed with black dashed lines. c Enlarged views of the boxed region around the OEC shown in b. Water molecules in the O1-channel and O4-channel

are shown as green and cyan spheres, respectively. The light blue mesh shows the radius of atoms of the OEC and water molecules in the O4-channel.

Fig. 2

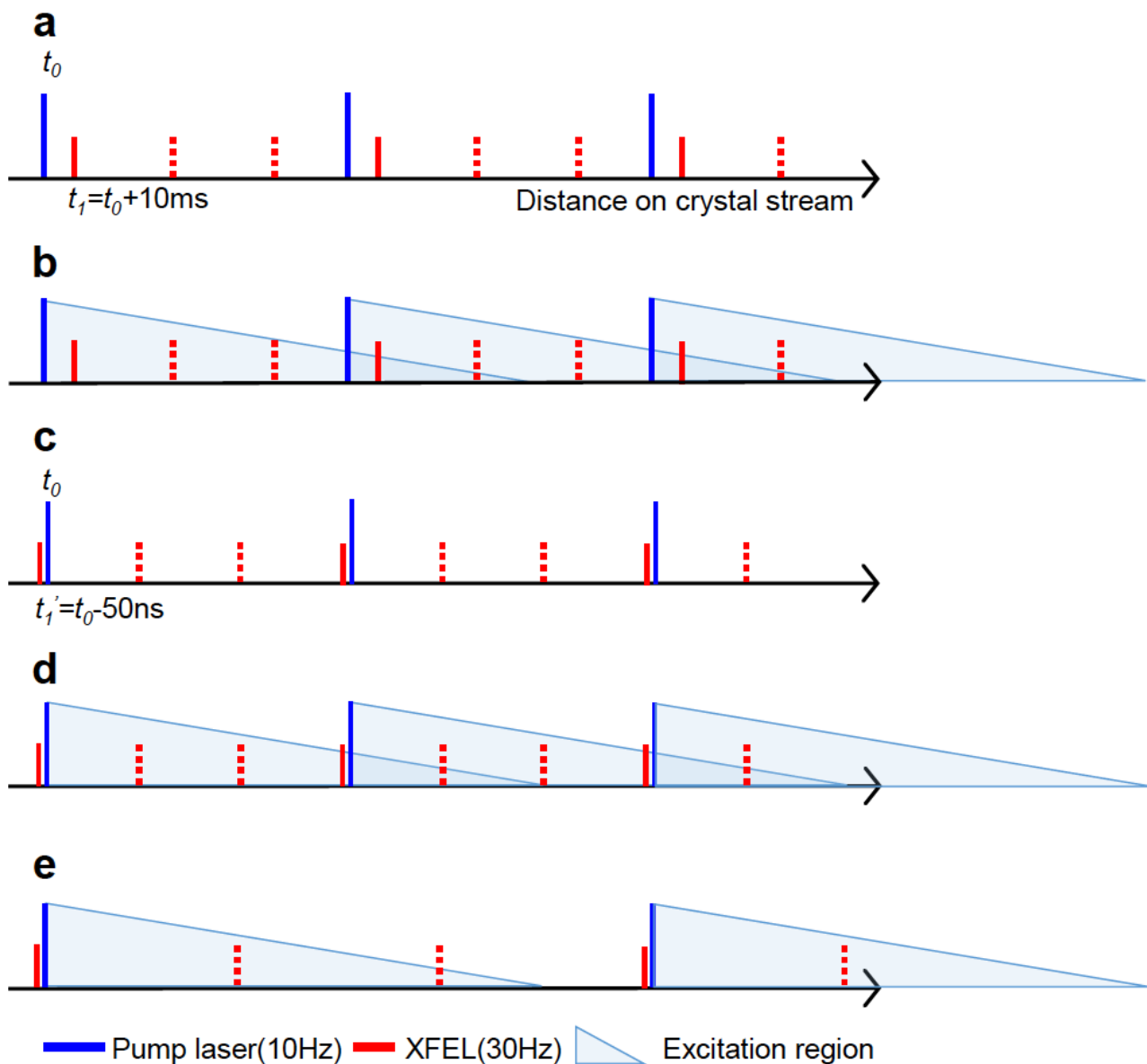


Figure 2

Schematic representation of the timing of the pump lasers and XFEL pulses. a, c Relative timing of the pump lasers and XFEL pulses with Δt of 10 ms (a) and Δt of -50 ns (c). b, d, e Schematic representations of the boundaries where the pump lasers reach at a slower flow rate with Δt of 10 ms (b) or with Δt of -50 ns (d), and that at a faster flow rate with Δt of -50 ns (e). Note that the region exposed to XFEL pulses

interact with multiple pump lasers when a slower flow rate was employed (b, d). XFEL pulses that were not recorded for the “light” datasets are shown as dash lines.

Fig. 3

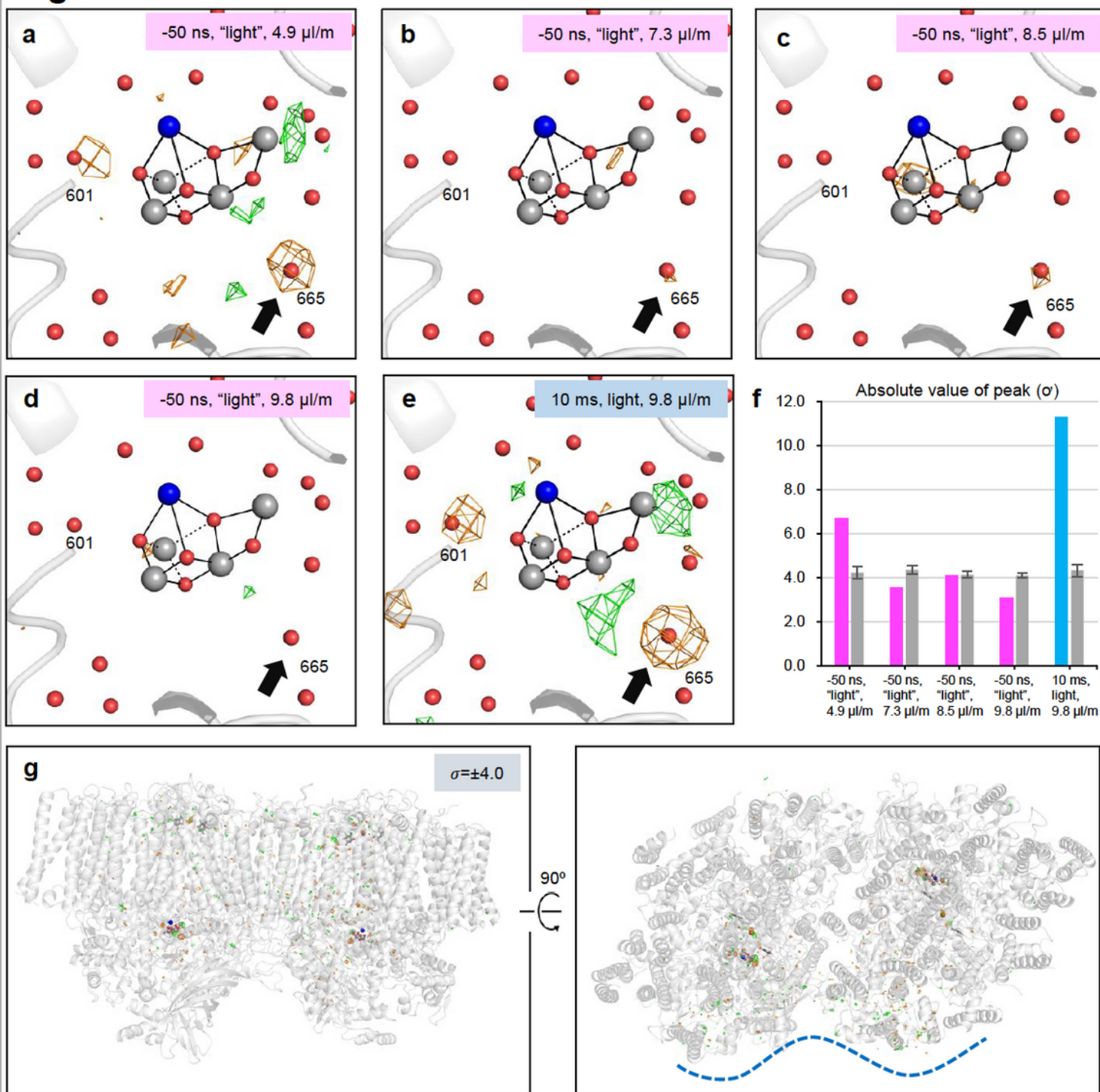


Figure 3

Light-induced structural changes in PSII observed at different flow rates. a-e The S1 state structure superimposed with Fobs(light) - Fobs(dark) isomorphous difference Fourier map contoured at $+4.0\sigma$ (green) and -4.0σ (orange) calculated with the “light” datasets obtained under conditions of (a) -50 ns,

“light”, 4.9 $\mu\text{l/m}$ flow rate, (b) -50 ns, “light”, 7.3 $\mu\text{l/m}$, (c) -50 ns, “light”, 8.5 $\mu\text{l/m}$, (d) -50 ns, “light”, 9.8 $\mu\text{l/m}$, and (e) 10 ms, light, 9.8 $\mu\text{l/m}$. The changes in W665 were indicated by black arrows. f Average peak heights of the difference map at the position of W665 calculated from two PSII monomers and maximum noises. Maximum noise levels with the error bar were calculated from five strongest noise peaks observed in the outside of PSII protein complex and shown in gray. g The overall PSII structure superposed with the difference map calculated with the dataset of 10 ms, light, 9.8 $\mu\text{l/m}$ at the same contour levels and color scheme as (e). The dimer interface where the minor structural changes distributed is indicated by a blue dashed line.

Fig. 4

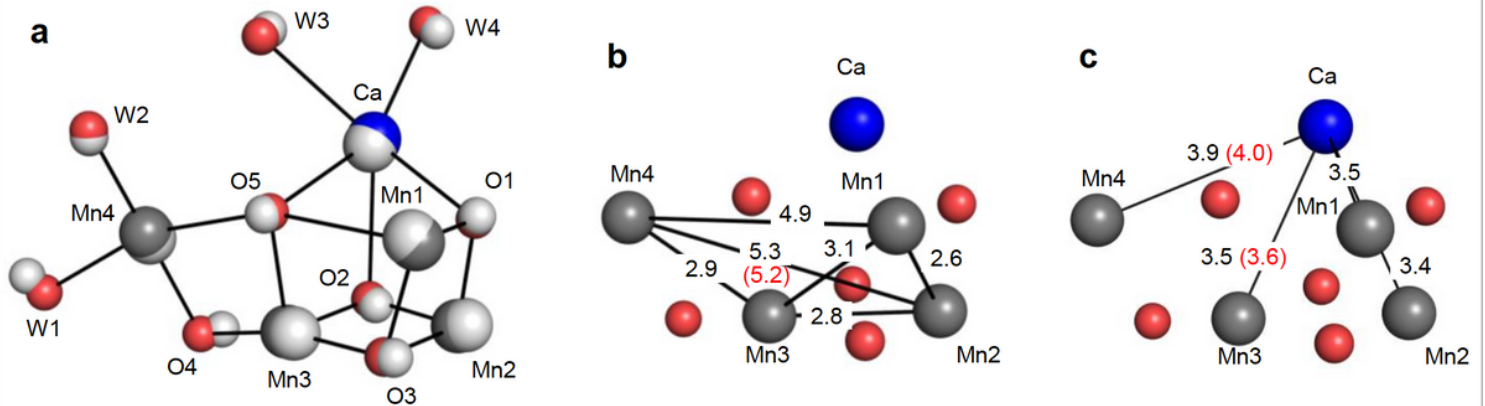


Figure 4

Structures of OEC in the S1 and S2 states. a-c OEC structures in the S1 and S2 states are shown in grey and colored atoms, respectively. Color codes: blue for calcium; cyan for manganese; red for oxygen. The color codes for the OEC are kept in all figures unless otherwise noted. In b, c, interatomic distances are shown in Å, with the numbers in black for S1 and red for S2, respectively. The distances in the S2 state were shown only when they are changed more than 0.1 Å compared with the corresponding distances in the S1 state.

Fig. 6

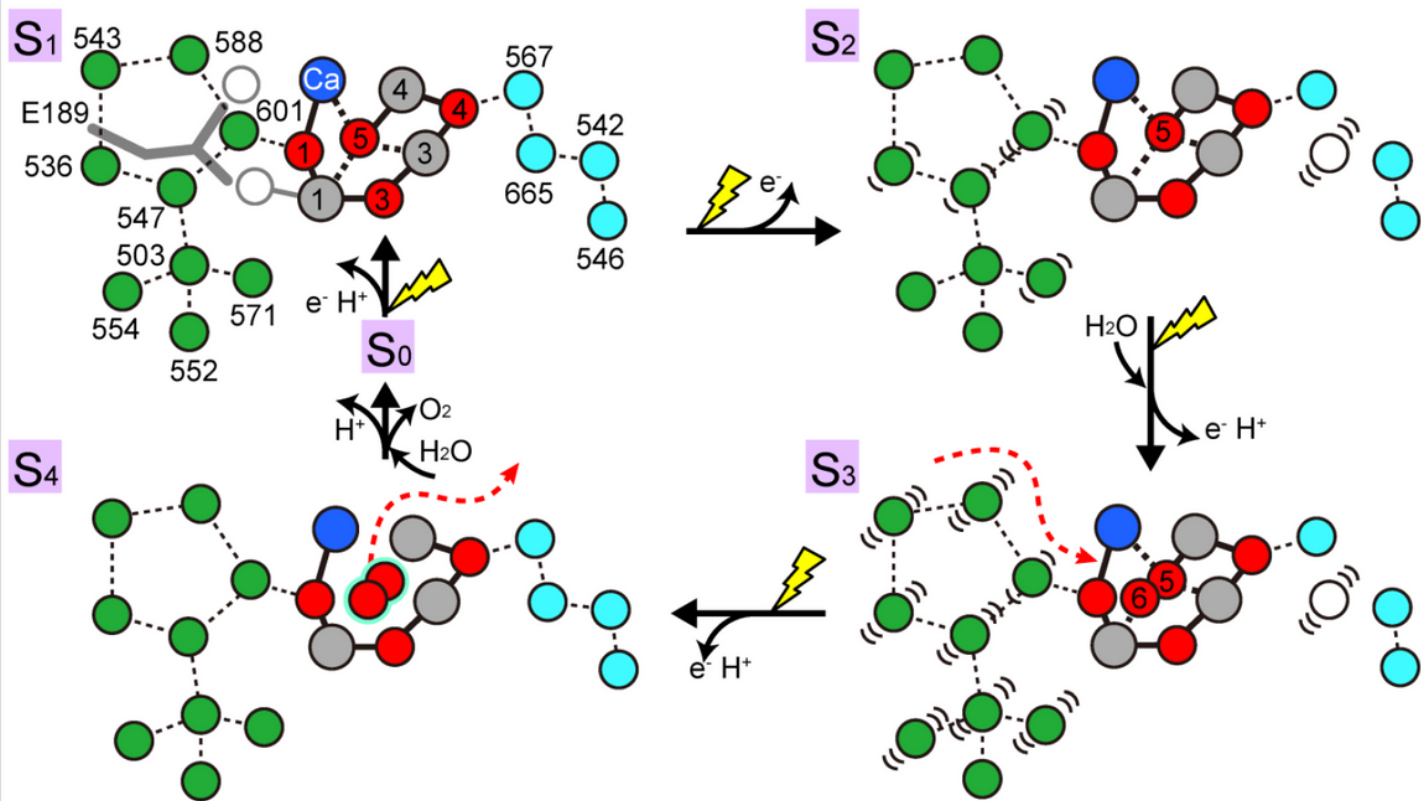


Figure 6

Structural changes in the water networks in the O1 and O4 channels during the water oxidation reaction. Structural changes in the OEC and water molecules found in the present and previous studies are summarized. Red and Gray spheres with numbers in the OEC were oxygen and manganese atoms, respectively, and the Mn2 and O2 atoms were omitted from the figure for clarity.